



Hot DA white dwarf model atmosphere calculations: including improved Ni PI cross-sections

S. P. Preval,^{1,2} M. A. Barstow,¹ N. R. Badnell,² I. Hubeny³ and J. B. Holberg⁴

¹Department of Physics and Astronomy, University of Leicester, University Road, Leicester LE1 7RH, UK

²Department of Physics, University of Strathclyde, Glasgow G4 0NG, UK

³Steward Observatory, University of Arizona, Tucson, AZ 85721, USA

⁴Lunar and Planetary Laboratory, Sonett Space Sciences Building, University of Arizona, Tucson, AZ 85721, USA

Accepted 2016 October 28. Received 2016 September 30; in original form 2015 November 20

ABSTRACT

To calculate realistic models of objects with Ni in their atmospheres, accurate atomic data for the relevant ionization stages need to be included in model atmosphere calculations. In the context of white dwarf stars, we investigate the effect of changing the Ni IV-VI bound-bound and bound-free atomic data on model atmosphere calculations. Models including photoionization cross-section (PICS) calculated with AUTOSTRUCTURE show significant flux attenuation of up to ~ 80 per cent shortward of 180 Å in the extreme ultraviolet (EUV) region compared to a model using hydrogenic PICS. Comparatively, models including a larger set of Ni transitions left the EUV, UV, and optical continua unaffected. We use models calculated with permutations of these atomic data to test for potential changes to measured metal abundances of the hot DA white dwarf G191-B2B. Models including AUTOSTRUCTURE PICS were found to change the abundances of N and O by as much as ~ 22 per cent compared to models using hydrogenic PICS, but heavier species were relatively unaffected. Models including AUTOSTRUCTURE PICS caused the abundances of N/O IV and v to diverge. This is because the increased opacity in the AUTOSTRUCTURE PICS model causes these charge states to form higher in the atmosphere, more so for N/O v . Models using an extended line list caused significant changes to the Ni IV-V abundances. While both PICS and an extended line list cause changes in both synthetic spectra and measured abundances, the biggest changes are caused by using AUTOSTRUCTURE PICS for Ni.

Key words: atomic data – opacity – white dwarfs.

1 INTRODUCTION

The presence of metals in white dwarf (WD) atmospheres can have dramatic effects on both the structure of the atmosphere, and the observed effective temperature (T_{eff}). For example, these effects have been demonstrated convincingly by Barstow, Hubeny & Holberg (1998). The authors determined the T_{eff} and surface gravity ($\log g$) of several hot DA WDs using a set of model atmosphere grids, which were either pure H and He, or heavy metal polluted. It was found that the T_{eff} determined using the pure H model grid was ≈ 4000 –7000 K higher than if a heavy metal-polluted model grid were used. Conversely, there was little to no difference in the measured $\log g$ when using either model grid.

It can be inferred that the completeness of the atomic data supplied in model calculations might have a significant effect on the measured T_{eff} . A study by Chayer, Fontaine & Wesemael (1995)

considered the effects of radiative levitation on the observed atmospheric metal abundances at different T_{eff} and $\log g$. In addition, these calculations were done using Fe data sets of varying line content. It was found that the number of transitions included in the calculation greatly affected the expected Fe abundance in the atmosphere (cf. Chayer et al. 1995, fig. 11). This result implies that the macroscopic quantities determined in a WD, such as metal abundance, are extremely sensitive to the input physics used to calculate the model grids. Therefore, this means that any atomic data that is supplied to the calculation must be as complete and accurate as possible in order to calculate the most representative model. While the Chayer et al. (1995) study considered only the variations in observed Fe abundance, it is reasonable to assume that the set of atomic data supplied may also have an impact on the T_{eff} and $\log g$ measured.

Studies of WD metal abundances, such as those of Barstow et al. (1998); Vennes & Lanz (2001); Preval et al. (2013), used model atmospheres incorporating the atomic data of Kurucz (1992, hereafter Ku92) in conjunction with photoionization cross-section (PICS)

* E-mail: simon.preval@strath.ac.uk

Table 1. The number of lines present in the [Ku92](#) and [Ku11](#) atomic databases for Fe and Ni IV–VII.

Ion	No of lines 1992	No of lines 2011
Fe IV	177 6984	146 172 28
Fe V	100 8385	778 5320
Fe VI	475 750	907 2714
Fe VII	902 50	291 6992
Ni IV	191 8070	151 526 36
Ni V	197 1819	156 224 52
Ni VI	221 1919	179 716 72
Ni VII	967 466	283 280 12
Total	104 206 43	111 467 026

data from the opacity project (OP) for Fe, and approximate hydrogenic PICS for Ni. A more comprehensive data set has since been calculated by Kurucz (2011, hereafter [Ku11](#)), containing a factor ~ 10 more transitions and energy levels for Fe and Ni IV–VI than its predecessor. In Table 1, we give a comparison of the number of Fe and Ni IV–VII transitions available between [Ku92](#) and [Ku11](#). In both the [Ku92](#) and [Ku11](#) data sets, the energy levels etc. were calculated using the Cowan Code (Cowan 1981). Based on the work discussed above, it is prudent to explore the differences between model atmospheres calculated using the [Ku92](#) and [Ku11](#) transition data, and the effect this has on measurements made using such models.

Ni V absorption features were first discovered in the hot DA WDs G191-B2B and REJ2214-492 by Holberg et al. (1994) using high-dispersion UV spectra from the International Ultraviolet Explorer. The authors derived Ni abundances of $\sim 1 \times 10^{-6}$ and $\sim 3 \times 10^{-6}$ as a fraction of H for G191-B2B and REJ2214-492, respectively. Compared to their measurements for Fe of $\sim 3 \times 10^{-5}$ and $\sim 1 \times 10^{-4}$ for G191-B2B and REJ2214-492, respectively, Ni is ~ 3 per cent of the Fe abundance for these stars. Werner & Dreizler (1994) also found Ni in two other hot DA WDs, namely Feige 24 and RE0623-377, measuring Ni abundances of $1 - 5 \times 10^{-6}$ and $1 - 5 \times 10^{-5}$, respectively. More recently, Preval et al. (2013) and Rauch et al. (2013) have measured Ni abundances for G191-B2B. Using Ni IV and V, Preval et al. (2013) found abundances of 3.24×10^{-7} and 1.01×10^{-6} , respectively, while Rauch et al. (2013) measured a single Ni abundance of 6×10^{-7} .

To date, there has been no attempt to include representative PICS for Ni in WD model atmosphere calculations. It is for this reason that we choose to focus on Ni and examine the effects of both including new PICS and transition data. We structure our paper as follows: We first describe the atomic data calculations required to generate PICS for Ni IV–VI. Next, we describe the model atmosphere calculations performed, and the tests we conducted. We then discuss the results. Finally, we state our conclusions.

2 ATOMIC DATA CALCULATIONS

The PICS data presented in this paper were calculated using the distorted wave atomic collision package [AUTOSTRUCTURE](#) (Badnell 1986, 1997, 2011). [AUTOSTRUCTURE](#) is an atomic structure package that can model several aspects of an arbitrary atom/ion *a priori*, including energy levels, transition oscillator strengths, electron-impact excitation cross-sections, PICS, and many others. [AUTOSTRUCTURE](#) is supplied with a set of configurations describing the number of electrons and the quantum numbers occupied for a

given atom or ion. The wavefunction P_{nl} for a particular configuration is obtained by solving the one particle Schrodinger equation

$$\left[\frac{d^2}{dr^2} - \frac{l(l+1)}{r^2} + 2V_{\text{Eff}}(r) + E_{nl} \right] P_{nl} = 0, \quad (1)$$

where n and l are the principle and orbital angular momentum quantum numbers, respectively, and V_{Eff} is an effective potential as described by Eissner & Nussbaumer (1969), which accounts for the presence of other electrons. Scaling parameters λ_{nl} can be included to scale the radial coordinate, which are related to the effective charge ‘seen’ by a particular valence electron, and typically has a value close to unity. The λ_{nl} can be varied according to the task. For an example, the parameters may be varied to minimize an energy functional, or they may be varied such that the difference between the calculated energy levels and a set of observed energy levels is minimized. Three coupling schemes are available in calculating the wavefunctions, dependent upon the resolution required, and the type of problem being considered. These are spin-orbit coupling (LS, term resolved), intermediate coupling (IC, level resolved), or configuration average (CA, configuration resolved).

We use IC with the aim of reproducing the energy levels from [Ku11](#) as closely as possible. The energy level structure is first determined by running [AUTOSTRUCTURE](#) with the configurations used by [Ku11](#), listed in Table 2. With this information, 17 λ_{nl} are then specified for orbitals 1s to 6s set initially to unity. The 1s parameter is fixed as it does not converge in the presence of relativistic corrections. The parameters were then varied to give as close agreement to the [Ku11](#) data as possible. The result of parameter variation is given in Table 3.

By comparing Table 1 with Table 2, it can be seen that the latter has more transitions than the former. This is because the transitions listed in [Ku11](#) are limited by their strength. Any observed/well-known transitions with $\log gf < -9.99$, or predicted transitions with a $\log gf < -7.5$ were omitted. In addition, the [Ku11](#) data base omitted radiative transitions between two autoionizing levels. We do the same. After calculating a set of scaling parameters for a particular ion, the accompanying PICS can be obtained. In order to see what potential effect (if any) replacing the hydrogenic PICS with more realistic data would have, we limited our calculations to considered direct photoionization (PI) only, neglecting resonances from photoexcitation/autoionization. The final photoionized configurations used in calculating the PICS were constructed by removing the outer most electron from each configuration in Table 4. These PI configurations are listed in Table 4. The PICS are evaluated for a table of 50 logarithmically spaced ejected electron energies spanning 0 to 100 Ryd. The PICS in the ejected electron energy frame are then linearly interpolated to the incident photon energy frame using two point interpolation.

[AUTOSTRUCTURE](#) employs the distorted wave method, which is an approximation. The calculations performed for the OP were done using an R-Matrix approach, which can potentially give the most accurate result in calculating PICS. Furthermore, the R-Matrix method automatically includes resonances arising from photoexcitation/autoionization, and interference between these two processes. In [AUTOSTRUCTURE](#), when the resonances are included separately, interference effects are neglected. The downside to use an R-Matrix calculation is the length of time and computer resources required to perform the calculation.

With regards to accuracy, Seaton & Badnell (2004) calculated term-resolved PI calculations for Fe VIII to Fe XIII using [AUTOSTRUCTURE](#). The authors then replaced data calculated for the OP, which consisted of R-Matrix plus [SUPERSTRUCTURE](#) (Eissner &

Table 2. Configurations prior to PI used in the AUTOSTRUCTURE calculations. Configurations in bold typeset represent the ground state configuration. The columns N_{config} , Levels, and Lines give the number of configurations used, and the number of energy levels and transitions generated, respectively.

Ion	Configurations	N_{config}	Levels	Lines
Ni iv	$\mathbf{3d^7}$, $3d^64s$, $3d^65s$, $3d^66s$, $3d^67s$, $3d^68s$ $3d^69s$, $3d^54s^2$, $3d^54s5s$, $3d^54s6s$, $3d^54s7s$, $3d^54s8s$ $3d^54s9s$, $3d^44s^25s$, $3d^44d$, $3d^65d$, $3d^66d$, $3d^67d$ $3d^68d$, $3d^69d$, $3d^54s4d$, $3d^54s5d$, $3d^54s6d$, $3d^54s7d$ $3d^54s8d$, $3d^54s9d$, $3d^44s^24d$, $3d^54p^2$, $3d^65g$, $3d^66g$ $3d^67g$, $3d^68g$, $3d^69g$, $3d^54s5g$, $3d^54s6g$, $3d^54s7g$ $3d^54s8g$, $3d^54s9g$, $3d^67i$, $3d^68i$, $3d^69i$, $3d^54s7i$ $3d^54s8i$, $3d^54s9i$ $3d^64p$, $3d^65p$, $3d^66p$, $3d^67p$, $3d^68p$, $3d^69p$ $3d^54s4p$, $3d^54s5p$, $3d^54s6p$, $3d^54s7p$, $3d^54s8p$, $3d^54s9p$ $3d^44s^24p$, $3d^64f$, $3d^65f$, $3d^66f$, $3d^67f$, $3d^68f$ $3d^69f$, $3d^54s4f$, $3d^54s5f$, $3d^54s6f$, $3d^54s7f$, $3d^54s8f$ $3d^54s9f$, $3d^44s^24f$, $3d^66h$, $3d^67h$, $3d^68h$, $3d^69h$ $3d^54s6h$, $3d^54s7h$, $3d^54s8h$, $3d^54s9h$, $3d^68k$, $3d^69k$ $3d^54s8k$, $3d^54s9k$, $3p^53d^8$	85	378 60	324 165 71
Ni v	$\mathbf{3d^6}$, $3d^54d$, $3d^55d$, $3d^56d$, $3d^57d$, $3d^58d$ $3d^59d$, $3d^510d$, $3d^44s4d$, $3d^44s5d$, $3d^44s6d$, $3d^44s7d$ $3d^44s8d$, $3d^44s9d$, $3d^44s10d$, $3d^54s$, $3d^55s$, $3d^56s$ $3d^57s$, $3d^58s$, $3d^59s$, $3d^510s$, $3d^44s^2$, $3d^44s5s$ $3d^44s6s$, $3d^44s7s$, $3d^44s8s$, $3d^44s9s$, $3d^44s10s$, $3d^55g$ $3d^56g$, $3d^57g$, $3d^58g$, $3d^59g$, $3d^44s5g$, $3d^44s6g$ $3d^44s7g$, $3d^44s8g$, $3d^44s9g$, $3d^57i$, $3d^58i$, $3d^59i$ $3d^44s7i$, $3d^44s8i$, $3d^44s9i$, $3d^44p^2$ $3d^54p$, $3d^55p$, $3d^56p$, $3d^57p$, $3d^58p$, $3d^59p$ $3d^510p$, $3d^44s4p$, $3d^44s5p$, $3d^44s6p$, $3d^44s7p$, $3d^44s8p$ $3d^44s9p$, $3d^44s10p$, $3d^34s^24p$, $3d^54f$, $3d^55f$, $3d^56f$ $3d^57f$, $3d^58f$, $3d^59f$, $3d^510f$, $3d^44s4f$, $3d^44s5f$ $3d^44s6f$, $3d^44s7f$, $3d^44s8f$, $3d^44s9f$, $3d^56h$, $3d^57h$ $3d^58h$, $3d^59h$, $3d^44s6h$, $3d^44s7h$, $3d^44s8h$, $3d^44s9h$ $3d^58k$, $3d^59k$, $3d^44s8k$, $3d^44s9k$, $3p^53d^8$	87	374 46	340 662 59
Ni vi	$\mathbf{3d^5}$, $3d^44d$, $3d^45d$, $3d^46d$, $3d^47d$, $3d^48d$ $3d^49d$, $3d^410d$, $3d^34s4d$, $3d^34s5d$, $3d^34s6d$, $3d^34s7d$ $3d^34s8d$, $3d^34s9d$, $3d^34s10d$, $3d^24s^24d$, $3d^24s^25d$, $3d^24s^26d$ $3d^24s^27d$, $3d^24s^28d$, $3d^24s^29d$, $3d^24s^210d$, $3d^44s$, $3d^45s$ $3d^46s$, $3d^47s$, $3d^48s$, $3d^49s$, $3d^410s$, $3d^34s^2$ $3d^34s5s$, $3d^34s6s$, $3d^34s7s$, $3d^34s8s$, $3d^34s9s$, $3d^34s10s$ $3d^24s^25s$, $3d^24s^26s$, $3d^24s^27s$, $3d^24s^28s$, $3d^24s^29s$, $3d^24s^210s$ $3d^45g$, $3d^46g$, $3d^47g$, $3d^48g$, $3d^49g$, $3d^410g$ $3d^34s5g$, $3d^34s6g$, $3d^34s7g$, $3d^34s8g$, $3d^34s9g$, $3d^34s10g$ $3d^47i$, $3d^48i$, $3d^49i$, $3d^34s7i$, $3d^34s8i$, $3d^34s9i$, $3d^34p^2$ $3d^44p$, $3d^45p$, $3d^46p$, $3d^47p$, $3d^48p$, $3d^49p$ $3d^410p$, $3d^411p$, $3d^34s4p$, $3d^34s5p$, $3d^34s6p$, $3d^34s7p$ $3d^34s8p$, $3d^34s9p$, $3d^34s10p$, $3d^34s11p$, $3d^24s^24p$, $3d^24s^25p$ $3d^24s^26p$, $3d^24s^27p$, $3d^24s^28p$, $3d^24s^29p$, $3d^24s^210p$, $3d^24s^211p$ $3d^44f$, $3d^45f$, $3d^46f$, $3d^47f$, $3d^48f$, $3d^49f$ $3d^410f$, $3d^411f$, $3d^34s4f$, $3d^34s5f$, $3d^34s6f$, $3d^34s7f$ $3d^34s8f$, $3d^34s9f$, $3d^34s10f$, $3d^34s11f$, $3d^24s^24f$, $3d^24s^25f$ $3d^24s^26f$, $3d^24s^27f$, $3d^24s^28f$, $3d^24s^29f$, $3d^24s^210f$, $3d^24s^211f$ $3d^46h$, $3d^47h$, $3d^48h$, $3d^49h$, $3d^34s6h$, $3d^34s7h$ $3d^34s8h$, $3d^34s9h$, $3d^48k$, $3d^49k$, $3d^34s8k$, $3d^34s9k$, $3p^53d^6$	122	293 66	424 128 22

Nussbaumer 1969) data for these ions, and re-evaluated the Rosseland means for a solar mixture. The Rosseland means calculated using the AUTOSTRUCTURE data were found to be close to those calculated with the OP data.

This implies that the distorted wave method is a good indicator of the potential effects of including new data. Therefore, it is instructive to perform such calculations before committing to a large R-Matrix calculation.

3 STELLAR ATMOSPHERE CALCULATIONS

All model atmospheres in this work were calculated using the non-local thermodynamic equilibrium (NLTE) stellar atmospheres code TLUSTY (Hubeny 1988; Hubeny & Lanz 1995), version 201. The models were then synthesized using SYNSPEC (Hubeny & Lanz 2011). TLUSTY benefits from the hybrid CL/ALI method, which combines the complete linearization (CL) and accelerated lambda iteration

Table 3. Calculated IC scaling parameters from AUTOSTRUCTURE.

Orbital	Ni IV	Ni V	Ni VI
2s	1.31391	1.31355	1.31487
2p	1.12294	1.12144	1.11996
3s	1.09887	1.11219	1.12750
3p	1.05876	1.07206	1.08779
3d	1.06828	1.09148	1.10379
4s	1.13492	1.15167	1.19770
4p	0.91520	0.90669	0.92207
4d	1.40156	1.48359	1.49036
4f	1.08824	1.03771	1.10538
5s	1.03946	1.03552	1.25294
5p	0.99302	0.96743	1.00439
5d	1.09409	1.08876	1.15671
5f	1.06373	1.01089	1.01693
5g	1.37199	1.17219	1.83712
6s	1.02002	1.01140	1.05828

Table 4. Final photoionized configurations used in the AUTOSTRUCTURE calculations.

Ion	Configurations
Ni IV	$3p^5 3d^7$, $3d^6$, $3d^5 4s$, $3d^5 4p$, $3d^4 4s^2$
Ni V	$3p^5 3d^6$, $3d^5$, $3d^4 4s$, $3d^4 4p$, $3d^3 4s^2$
Ni VI	$3d^4$, $3p^5 3d^5$, $3d^3 4s$, $3d^3 4p$, $3d^2 4s^2$

(ALI) methods in order to accelerate the rate of convergence of a model. `TLUSTY` has two methods in which to treat heavy metal opacity, namely opacity distribution functions, and opacity sampling (OS). Nominally, OS is a Monte Carlo sampling method. However, in the limit of high resolution, OS is an exact method for accounting for opacity. We use OS, and specify a resolution of five fiducial¹ Doppler widths.

As the [Ku11](#) data contains more energy levels than [Ku92](#), we constructed new model ions for Ni IV–VI according to the prescription of [Anderson \(1989\)](#); however, superlevels were calculated using energies of either even or odd parity. If we created superlevels with a mixture of even or odd levels, then we would have to consider transitions between levels within the superlevel (cf. [Hubeny & Lanz 1995](#)). The Ni IV–VI ions have 73, 90, and 75 superlevels, respectively. The PICS for each superlevel $\bar{\sigma}_{\text{PI}}(E_\gamma)$ as a function of photon energy E_γ were calculated as an average of the PICS for each individual level $\sigma_i(E)$ used to create the superlevel, weighted by the statistical weights of each level g_i . This can be written as

$$\bar{\sigma}_{\text{PI}}(E_\gamma) = \frac{\sum_{i=1}^N \sigma_i(E_\gamma) g_i}{\sum_{i=1}^N g_i}, \quad (2)$$

where N is the number of levels used to form the superlevel. We refer to these summed PICS as supercross-sections hereafter. In Fig. 1, we have plotted the total supercross-sections for Ni IV–VI for both the hydrogenic and `AUTOSTRUCTURE` cases. Prior to summation, each supercross-section was multiplied by a Boltzmann constant. It can be seen that the total supercross-sections calculated in `AUTOSTRUCTURE` are far larger than their hydrogenic counterparts.

As there are two different Ni line lists ([Ku92](#) and [Ku11](#)), and two different sets of PICS (hydrogenic and those calculated with `AUTOSTRUCTURE`), there are four different combinations that we can

¹ the Doppler width for Fe absorption features at T_{eff} .

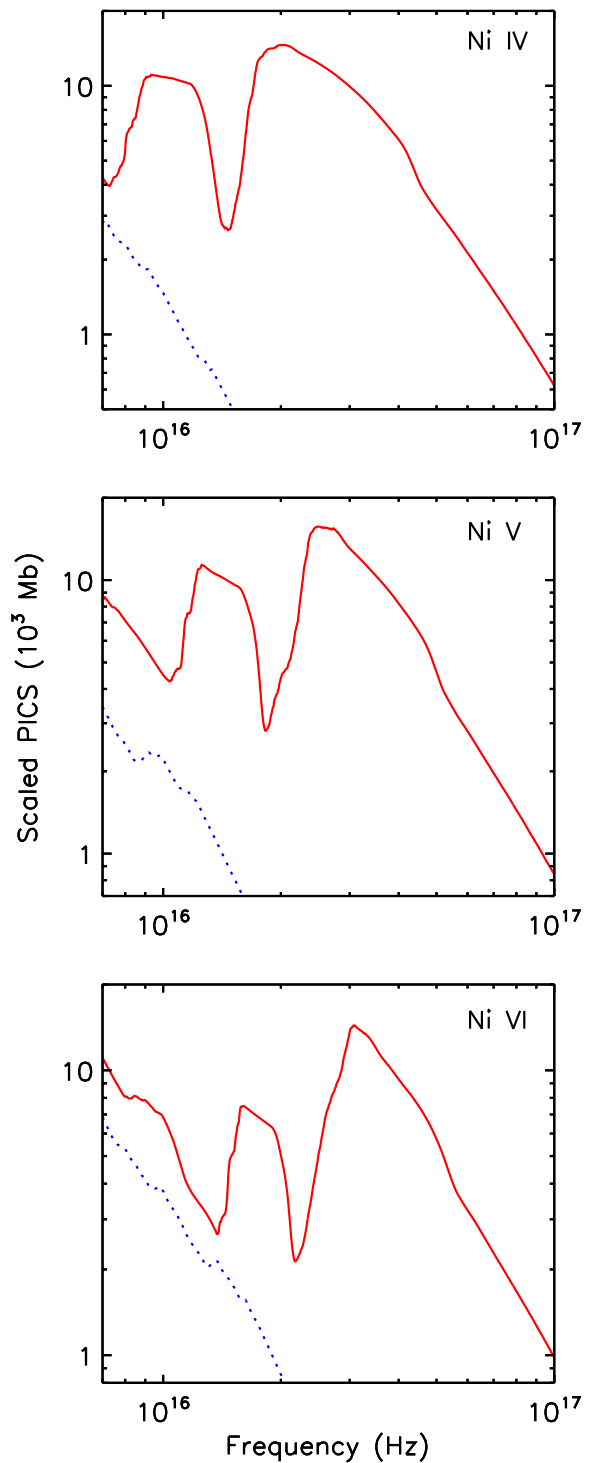


Figure 1. Plot of summed supercross-sections for Ni IV–VI calculated using `AUTOSTRUCTURE` (solid red) and a hydrogenic approximation (dotted blue). Prior to addition, each supercross-section was weight by a Boltzmann factor and the statistical weight of the superlevel concerned.

test. Therefore, we calculated four different models in NLTE. We refer to these as Models 1, 2, 3, and 4. In Model 1, we use the [Ku92](#) transitions and hydrogenic PICS. In Model 2, we use the [Ku11](#) transitions and hydrogenic PICS. In Model 3, we use the [Ku92](#) transitions and `AUTOSTRUCTURE` PICS. Finally, in Model 4, we use the [Ku11](#) transitions and `AUTOSTRUCTURE` PICS. In all four cases, we

Table 5. Metal abundances used in calculating the four model atmospheres described in text as a fraction of H. These abundances originate from Preval et al. (2013), where the values with the lowest statistical uncertainty were used.

Metal	Abundance X/H
He	1.00×10^{-5}
C	1.72×10^{-7}
N	2.16×10^{-7}
O	4.12×10^{-7}
Al	1.60×10^{-7}
Si	3.68×10^{-7}
P	1.64×10^{-8}
S	1.71×10^{-7}
Fe	1.83×10^{-6}
Ni	1.01×10^{-6}

based the models on a G191-B2B like atmosphere, and calculated the models with $T_{\text{eff}} = 525\,000$ K, $\log g = 7.53$ (Barstow et al. 2003), and metal abundances listed in Table 5. These abundances were taken from Preval et al. (2013), measured in their analysis of the hot DA WD G191-B2B. In the case where there was more than one ionization stage considered, we used the abundances with the smallest uncertainty. Listed in Table 6 are the model ions used in TLUSTY, along with the number of superlevels included.

3.1 Spectral energy distribution

For this comparison, we considered the differences between the spectral energy distributions (SED) of each model. For each model, we synthesize three spectra covering the extreme ultraviolet (EUV), the ultraviolet (UV), and the optical regions. We then calculated the residual between Models 1 and 2, 1 and 3, and 1 and 4 using the equation

$$\text{Residual} = \frac{F_i - F_1}{F_1}, \quad (3)$$

where F_1 is the flux for Model 1, and F_i is the flux for Model 2, 3, or 4.

3.2 Abundance variations

For this comparison, we wanted to examine the differences between abundances measured for G191-B2B when using each of the four models described above. Using a similar method to Preval et al. (2013), we measured the abundances for G191-B2B using all four of the models described above. The observational data for G191-B2B consists of three high S/N spectra constructed by co-adding multiple data sets. The first spectrum uses data from the Far Ultraviolet Spectroscopic Explorer spanning 910–1185 Å, and the other two use data from the Space Telescope Imaging Spectrometer aboard the *Hubble Space Telescope* spanning 1160–1680 Å and 1625–3145 Å, respectively. A full list of the data sets used, and the coaddition procedure, is given in detail in Preval et al. (2013).

The model grids for each metal was constructed by using SYNSPEC. SYNSPEC takes a starting model converged assuming NLTE, and is able to calculate a spectrum for smaller or larger metal abundances by stepping away in LTE. We used the X-ray spectral package XSPEC (Arnaud 1996) to measure the abundances. XSPEC takes a grid of models and observational data and interpolates between these

Table 6. List of model ions and the number of levels used in model atmosphere calculations described in the text. Ions marked with * were treated approximately as single level ions by TLUSTY. For Ni, the number of levels outside and inside the brackets correspond to the number of levels for the Ku92 and Ku11 model ions, respectively.

Ion	N superlevels
H I	9
H II*	1
He I	24
He II	20
He III*	1
C III	23
C IV	41
C V*	1
N III	32
N IV	23
N V	16
N VI*	1
O IV	39
O V	40
O VI	20
O VII*	1
Al III	23
Al IV*	1
Si III	30
Si IV	23
Si V*	1
P IV	14
P V	17
P VI*	1
S IV	15
S V	12
S VI	16
S VII*	1
Fe IV	43
Fe V	42
Fe VI	32
Fe VII*	1
Ni IV	38 (73)
Ni V	48 (90)
Ni VI	42 (75)
Ni VII*	1

models using a chi square (χ^2) minimization procedure. XSPEC is unable to use observational data with a large number of data points. To remedy this, we isolate individual absorption features for various ions and then use XSPEC to measure the abundances. A full list of the absorption features used and the sections of spectrum extracted is given in table 9 in Preval et al. (2013). In addition to this list, we also include measurements of the O V abundance using the excited transition with wavelength 1371.296 Å.

4 RESULTS AND DISCUSSION.

Here, we discuss the results obtained from the four models calculated using permutations of the Ku92 and Ku11 atomic data, and the hydrogenic and AUTOSTRUCTURE cross-section data. Models 1, 2, 3, and 4 used Ku92/hydrogenic, Ku11/hydrogenic, Ku92/AUTOSTRUCTURE, and Ku11/AUTOSTRUCTURE, respectively.

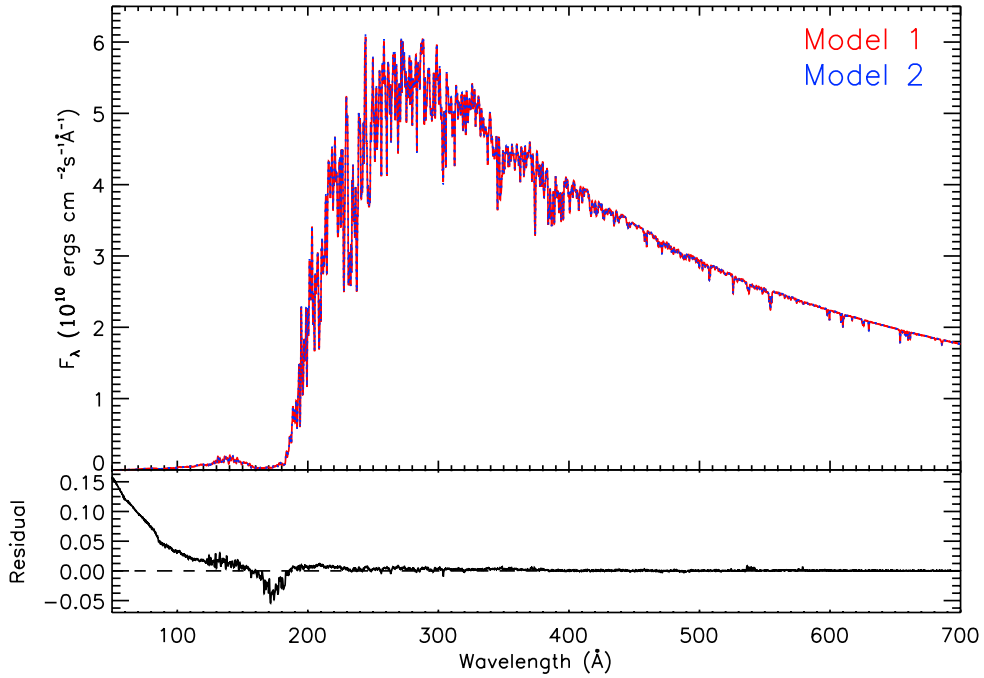


Figure 2. Plot of the EUV region covering 50–700 Å synthesized for Models 1 (red solid) and 2 (blue dotted). On the bottom is a plot of the residual between the two models. The dashed line indicates a residual of zero, or no difference.

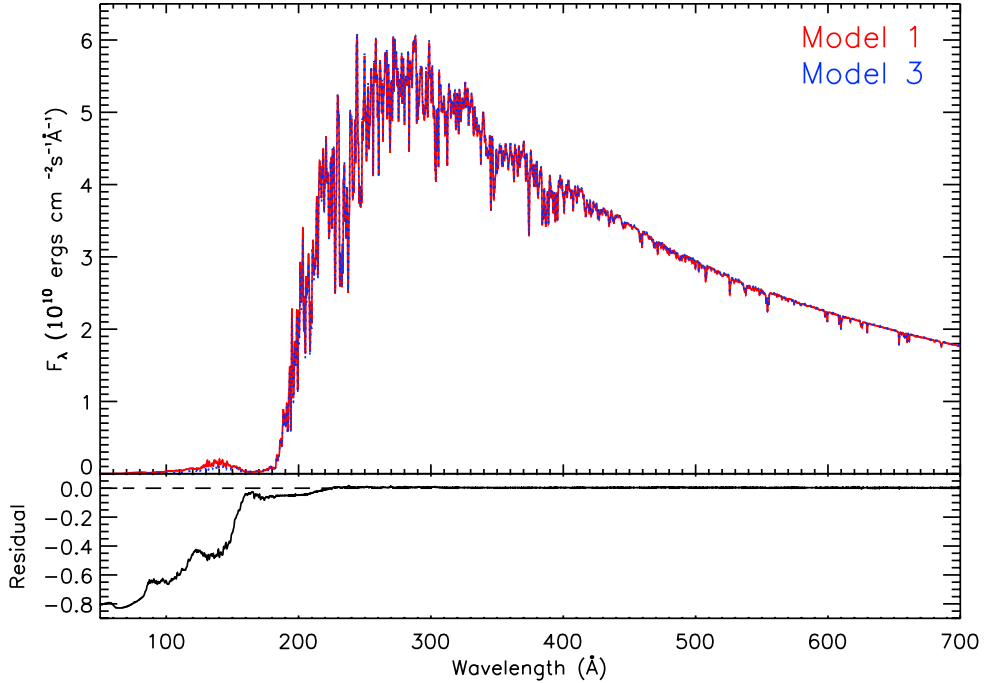


Figure 3. Same as Fig. 2, but for Models 1 and 3.

4.1 SED variations

In this subsection, we discuss the differences between spectra synthesized for the four models described above.

4.1.1 EUV

Of all the spectral regions, the EUV undergoes the most dramatic changes. However, the EUV region appears to be relatively in-

sensitive to whether [Ku92](#) or [Ku11](#) is used. In Fig. 2, we have plotted the EUV region for Models 1 and 2, along with the residual between these two models as defined in text. Below 200 Å the flux of Model 2 appears to increase as wavelength decreases, being ~ 15 per cent larger by 50 Å. This may be due to how the superlevels are partitioned in the model calculation rather than a decrease in opacity from the [Ku11](#) line list. In Fig. 3, we plot the same region, but with Models 1 and 3. Significant changes occur below 180 Å, with the flux of Model 3 being greatly attenuated,

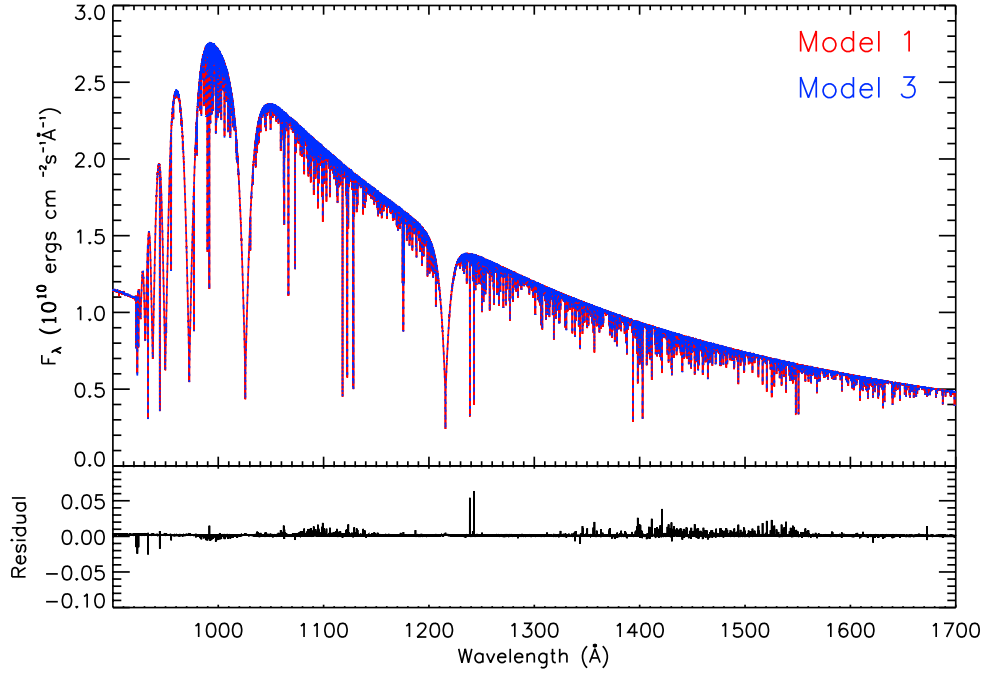


Figure 4. Plot of the UV region covering 910–1700 Å synthesized for Models 1 (red solid) and 2 (blue dotted). On the bottom is a plot of the residual between the two models. The dashed line indicates a residual of zero, or no difference.

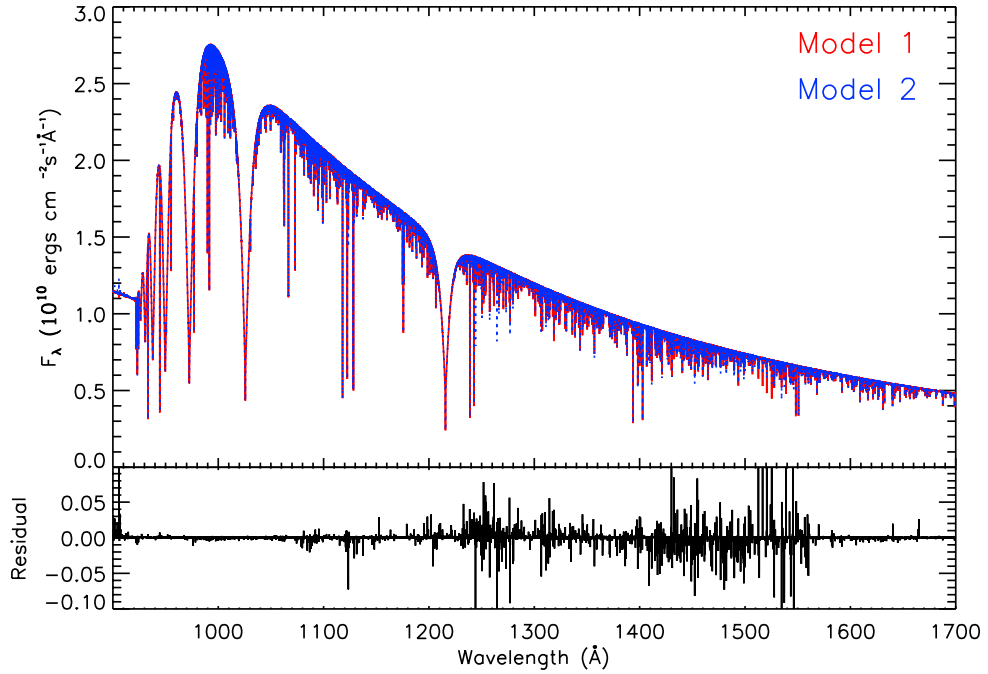


Figure 5. Same as Fig. 4, but for Models 1 (red solid) and 3 (blue dotted).

reaching a maximum of ~ 80 per cent with respect to Model 1. This is indicative of a larger opacity due to the AUTOSTRUCTURE PICS for Ni. Model 4 showed a combination of effects from Models 2 and 3.

4.1.2 UV

In the case of the UV region, not a lot changes when using the AUTOSTRUCTURE PICS. In Fig. 4, we have plotted synthetic spectra for Models 1 and 3 in the UV region. It can be seen that changes are

limited to absorption features only, with the vast majority only changing depth by ~ 3 per cent. The obvious exception to this is the Nv doublet near 1240 Å, where the depth has changed by ~ 5 –6 per cent. In Fig. 5, we have now plotted Models 1 and 2. Again, changes are limited to absorption features, but these are now far more pronounced, with depth changes of up to and beyond 10 per cent. These features can be attributed to Ni, and a few lighter metals, the abundances of which we discuss later. Again, Model 4 showed a combination of the changes seen in Models 2 and 3.

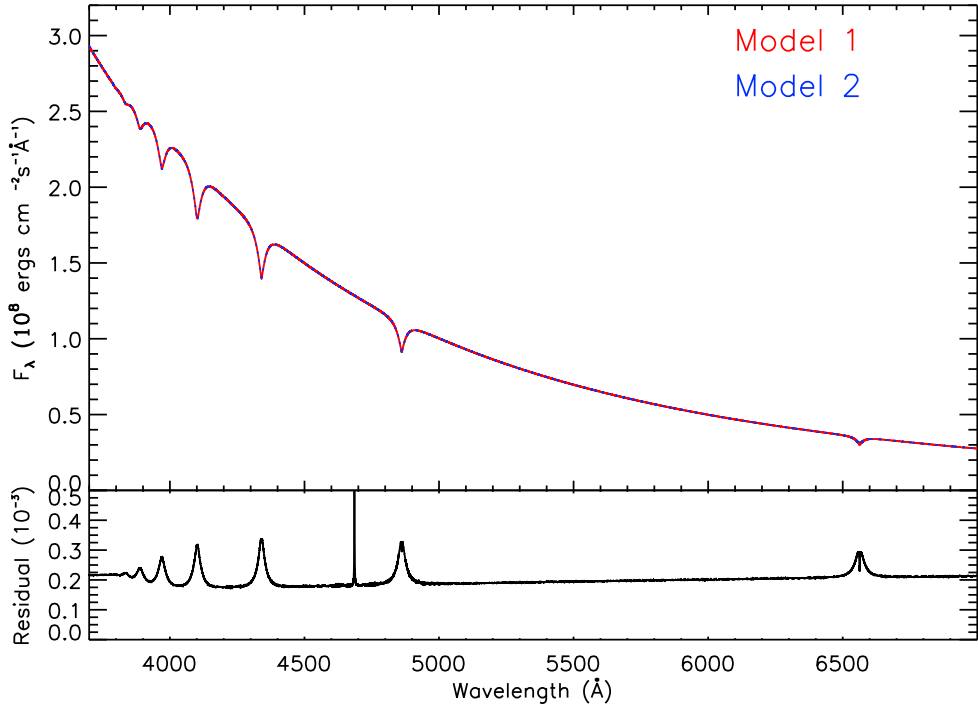


Figure 6. Plot of the optical region covering 3800–7000 Å synthesized for Models 1 (red solid) and 2 (blue dotted). On the bottom is a plot of the residual between the two models. The sharp residual at 4690 Å is due to the He II 4860.677 Å transition.

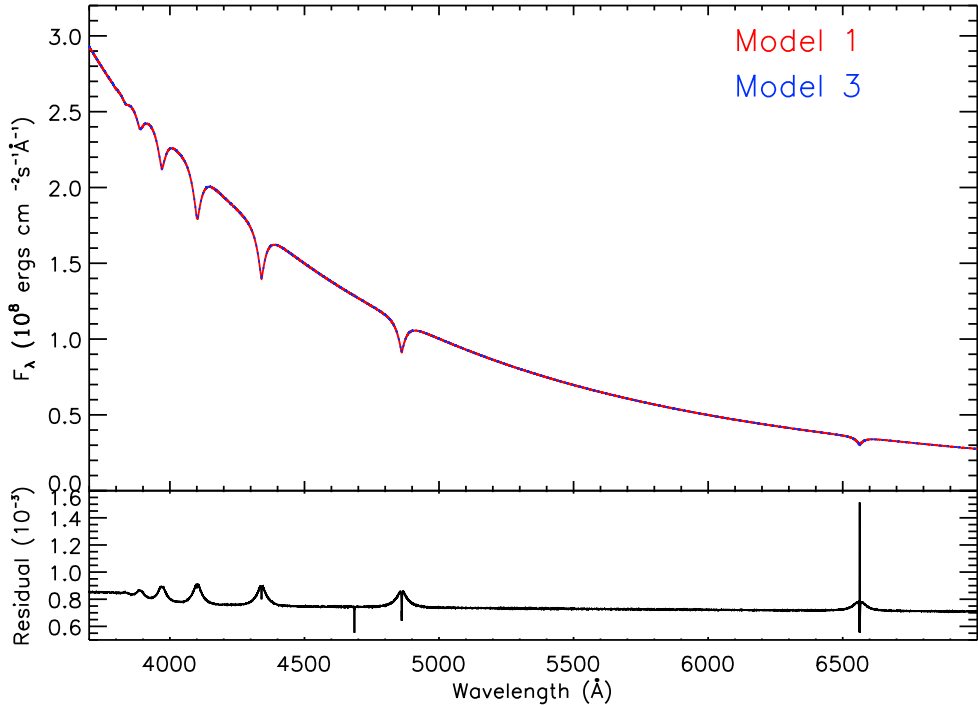


Figure 7. Same as Fig. 6, but for Models 1 (red solid) and 3 (blue dotted).

4.1.3 Optical

Very little to no change occurs in the optical region, regardless of line list or PICS used to calculate the models. In Figs 6 and 7, we plot the synthetic spectra of Models 1 and 2, and 1 and 3 in the optical region, respectively. In both cases, changes to both the continuum flux and the H-balmer lines can be seen, but these are restricted to <0.1 per cent. The same also occurs for Model 4. Because these

changes are so small, it is highly unlikely that measurements made using these models would be significantly different.

4.2 Abundance measurements

In Table 7, we list the abundance measurements made using the various models. We have also given the abundance differences

Table 7. Summary of the abundances measured as a number fraction of H. The 1–2, 1–3, and 1–4 columns give the difference between abundances measured using these models. The Σ column gives the sum of the 1–2 and 1–3 columns. Differences typeset in italics are statistically significant (i.e. consistent with a non-zero difference). Note $[x] = 1 \times 10^x$

Ion	Model 1	Model 2	Model 3	Model 4	1–2	1–3	1–4	Σ
C III	$1.83^{+0.03}_{-0.03}[-7]$	$1.83^{+0.03}_{-0.03}[-7]$	$1.83^{+0.03}_{-0.03}[-7]$	$1.83^{+0.03}_{-0.03}[-7]$	$0.00^{+0.04}_{-0.04}[-7]$	$0.00^{+0.04}_{-0.04}[-7]$	$0.00^{+0.04}_{-0.04}[-7]$	$0.00^{+0.06}_{-0.06}[-7]$
C IV	$3.00^{+0.10}_{-0.14}[-7]$	$3.00^{+0.10}_{-0.17}[-7]$	$3.00^{+0.10}_{-0.17}[-7]$	$3.00^{+0.09}_{-0.20}[-7]$	$0.00^{+0.14}_{-0.22}[-7]$	$0.00^{+0.15}_{-0.22}[-7]$	$0.00^{+0.14}_{-0.24}[-7]$	$0.00^{+0.21}_{-0.31}[-7]$
N IV	$1.67^{+0.22}_{-0.22}[-7]$	$1.65^{+0.22}_{-0.22}[-7]$	$1.62^{+0.22}_{-0.22}[-7]$	$1.60^{+0.22}_{-0.22}[-7]$	$0.02^{+0.31}_{-0.31}[-7]$	$0.05^{+0.31}_{-0.31}[-7]$	$0.07^{+0.31}_{-0.31}[-7]$	$0.07^{+0.44}_{-0.44}[-7]$
N V	$1.65^{+0.02}_{-0.02}[-7]$	$1.77^{+0.02}_{-0.02}[-7]$	$1.87^{+0.02}_{-0.02}[-7]$	$1.99^{+0.02}_{-0.02}[-7]$	$-0.12^{+0.02}_{-0.02}[-7]$	$-0.23^{+0.02}_{-0.02}[-7]$	$-0.35^{+0.02}_{-0.02}[-7]$	$-0.35^{+0.03}_{-0.03}[-7]$
O IV	$4.63^{+0.12}_{-0.12}[-7]$	$4.54^{+0.12}_{-0.12}[-7]$	$4.38^{+0.12}_{-0.12}[-7]$	$4.31^{+0.12}_{-0.12}[-7]$	$0.09^{+0.17}_{-0.17}[-7]$	$0.25^{+0.17}_{-0.17}[-7]$	$0.32^{+0.17}_{-0.17}[-7]$	$0.34^{+0.24}_{-0.24}[-7]$
O V	$1.47^{+0.07}_{-0.07}[-6]$	$1.56^{+0.07}_{-0.07}[-6]$	$1.69^{+0.08}_{-0.08}[-6]$	$1.79^{+0.08}_{-0.08}[-6]$	$-0.09^{+0.10}_{-0.10}[-6]$	$-0.23^{+0.10}_{-0.10}[-6]$	$-0.32^{+0.11}_{-0.11}[-6]$	$-0.32^{+0.14}_{-0.14}[-6]$
Al III	$1.62^{+0.09}_{-0.09}[-7]$	$1.63^{+0.10}_{-0.10}[-7]$	$1.63^{+0.10}_{-0.10}[-7]$	$1.63^{+0.10}_{-0.10}[-7]$	$-0.01^{+0.13}_{-0.13}[-7]$	$-0.01^{+0.13}_{-0.13}[-7]$	$-0.01^{+0.13}_{-0.13}[-7]$	$-0.02^{+0.18}_{-0.18}[-7]$
Si III	$2.90^{+0.39}_{-0.23}[-7]$	$2.89^{+0.38}_{-0.23}[-7]$	$2.92^{+0.41}_{-0.23}[-7]$	$2.92^{+0.41}_{-0.23}[-7]$	$0.00^{+0.54}_{-0.32}[-7]$	$-0.02^{+0.57}_{-0.33}[-7]$	$-0.02^{+0.56}_{-0.33}[-7]$	$-0.02^{+0.79}_{-0.46}[-7]$
Si IV	$3.32^{+0.20}_{-0.20}[-7]$	$3.33^{+0.20}_{-0.20}[-7]$	$3.34^{+0.20}_{-0.20}[-7]$	$3.35^{+0.20}_{-0.20}[-7]$	$-0.01^{+0.28}_{-0.28}[-7]$	$-0.02^{+0.28}_{-0.28}[-7]$	$-0.03^{+0.28}_{-0.28}[-7]$	$-0.03^{+0.40}_{-0.40}[-7]$
P IV	$1.34^{+0.20}_{-0.20}[-7]$	$1.34^{+0.20}_{-0.20}[-7]$	$1.30^{+0.19}_{-0.20}[-7]$	$1.30^{+0.19}_{-0.20}[-7]$	$0.00^{+0.28}_{-0.28}[-7]$	$0.03^{+0.28}_{-0.28}[-7]$	$0.04^{+0.28}_{-0.28}[-7]$	$0.03^{+0.40}_{-0.40}[-7]$
P V	$1.91^{+0.03}_{-0.03}[-8]$	$1.91^{+0.03}_{-0.03}[-8]$	$1.91^{+0.03}_{-0.03}[-8]$	$1.90^{+0.03}_{-0.03}[-8]$	$0.01^{+0.04}_{-0.04}[-8]$	$0.00^{+0.04}_{-0.04}[-8]$	$0.01^{+0.04}_{-0.04}[-8]$	$0.01^{+0.06}_{-0.06}[-8]$
S IV	$2.01^{+0.03}_{-0.03}[-7]$	$1.99^{+0.03}_{-0.03}[-7]$	$1.99^{+0.03}_{-0.03}[-7]$	$1.96^{+0.03}_{-0.03}[-7]$	$0.03^{+0.05}_{-0.05}[-7]$	$0.02^{+0.05}_{-0.05}[-7]$	$0.05^{+0.05}_{-0.05}[-7]$	$0.05^{+0.07}_{-0.07}[-7]$
S VI	$7.55^{+0.20}_{-0.20}[-8]$	$7.64^{+0.20}_{-0.20}[-8]$	$7.51^{+0.20}_{-0.20}[-8]$	$7.59^{+0.20}_{-0.20}[-8]$	$-0.08^{+0.28}_{-0.28}[-8]$	$0.05^{+0.28}_{-0.28}[-8]$	$-0.03^{+0.28}_{-0.28}[-8]$	$-0.03^{+0.40}_{-0.40}[-8]$
Fe IV	$2.05^{+0.04}_{-0.04}[-6]$	$2.01^{+0.04}_{-0.04}[-6]$	$2.02^{+0.04}_{-0.04}[-6]$	$1.98^{+0.04}_{-0.04}[-6]$	$0.04^{+0.05}_{-0.05}[-6]$	$0.03^{+0.05}_{-0.05}[-6]$	$0.07^{+0.05}_{-0.05}[-6]$	$0.07^{+0.07}_{-0.07}[-6]$
Fe V	$5.37^{+0.08}_{-0.08}[-6]$	$5.31^{+0.07}_{-0.07}[-6]$	$5.27^{+0.07}_{-0.07}[-6]$	$5.20^{+0.07}_{-0.07}[-6]$	$0.06^{+0.11}_{-0.11}[-6]$	$0.10^{+0.11}_{-0.11}[-6]$	$0.17^{+0.11}_{-0.11}[-6]$	$0.16^{+0.16}_{-0.16}[-6]$
Ni IV	$3.00^{+0.09}_{-0.04}[-7]$	$2.81^{+0.05}_{-0.05}[-7]$	$3.32^{+0.10}_{-0.10}[-7]$	$2.97^{+0.12}_{-0.05}[-7]$	$0.19^{+0.10}_{-0.06}[-7]$	$-0.32^{+0.13}_{-0.10}[-7]$	$0.03^{+0.15}_{-0.07}[-7]$	$-0.13^{+0.16}_{-0.12}[-7]$
Ni V	$9.88^{+0.28}_{-0.21}[-7]$	$1.22^{+0.04}_{-0.04}[-6]$	$9.81^{+0.23}_{-0.21}[-7]$	$1.20^{+0.04}_{-0.04}[-6]$	$-2.30^{+0.29}_{-0.22}[-7]$	$0.06^{+0.37}_{-0.30}[-7]$	$-2.12^{+0.29}_{-0.22}[-7]$	$-2.24^{+0.47}_{-0.37}[-7]$

between Models 1 and 2, 1 and 3, and 1 and 4. Seven ions were found to have statistically significant abundance differences dependent on which model was used, namely N V, O IV, O V, Fe IV, Fe V, Ni IV, and Ni V.

4.2.1 N V

For N V, significant changes are seen in Models 2, 3, and 4. Using Model 1, we measured the abundance of N V to be $1.65^{+0.02}_{-0.02} \times 10^{-7}$, whereas for Models 2, 3, and 4, we find $1.77^{+0.02}_{-0.02} \times 10^{-7}$, $1.87^{+0.02}_{-0.02} \times 10^{-7}$, and $1.99^{+0.02}_{-0.02} \times 10^{-7}$, respectively. The abundances measured using Models 2, 3, and 4 correspond to increases from Model 1 of ~ 7 per cent, ~ 13 per cent, and ~ 20 per cent, respectively. This suggests that both the number of transitions and the PICS used cause significant changes to the abundance.

4.2.2 O IV–V

In the case of O IV, significant changes in the abundances are seen when using the AUTOSTRUCTURE PICS in Models 3 and 4. For O IV, we measured the abundance to be $4.63^{+0.12}_{-0.12} \times 10^{-7}$ using Model 1. For Models 3 and 4, we measured abundances of $4.38^{+0.12}_{-0.12} \times 10^{-7}$ and $4.31^{+0.12}_{-0.12} \times 10^{-7}$, respectively, corresponding to decreases of ~ 5 per cent and ~ 7 per cent, respectively.

A similar case occurs for O V, where statistically significant differences occur for Models 3 and 4. Using Model 1, we measured an abundance of $1.47^{+0.07}_{-0.07} \times 10^{-6}$, whereas for Models 3 and 4 we measured abundances of $1.69^{+0.08}_{-0.08} \times 10^{-6}$ and $1.79^{+0.08}_{-0.08} \times 10^{-6}$, respectively. This corresponds to an increase of ~ 15 per cent and ~ 22 per cent for Models 3 and 4 over Model 1, respectively. These

results suggest that the largest changes to the O IV–V may be caused by the PICS rather than the number of transitions included in the line list.

4.2.3 Fe IV–V

The Fe IV–V abundances appear relatively insensitive to changes in the line list used and the PICS. A statistically significant difference was only observed between abundances measured using Models 1 and 4. For Fe IV, we measured an abundance of $2.05^{+0.04}_{-0.04} \times 10^{-6}$ for Model 1, and $1.98^{+0.04}_{-0.04} \times 10^{-6}$ for Model 4. This is an ~ 3 per cent decrease from Model 1. For Fe V, we measured abundances of $5.37^{+0.08}_{-0.08} \times 10^{-6}$ and $5.20^{+0.07}_{-0.07} \times 10^{-6}$ for Models 1 and 4, respectively, corresponding to an ~ 3 per cent decrease. These changes appear to suggest that a combination of both the number of transitions and PICS is required to change the abundance. We discuss this further below.

4.2.4 Ni IV–V

Interestingly, statistically significant changes compared to Model 1 are seen in the Ni IV abundance when Models 2 and 3 are used, but not for Model 4. For Model 1, we measured the abundance to be $3.00^{+0.09}_{-0.04} \times 10^{-7}$. For Models 2 and 3, we measure the abundances to be $2.81^{+0.05}_{-0.05} \times 10^{-7}$ and $3.32^{+0.10}_{-0.10} \times 10^{-7}$, respectively. This corresponds to a decrease of ~ 6 per cent for Model 2, and an increase of ~ 11 per cent for Model 3. In the case of Model 4, an abundance of $2.97^{+0.12}_{-0.05} \times 10^{-7}$ was measured.

The Ni V abundance appears to depend strongly upon whether Ku92 or Ku11 atomic data were included. In Model 1, an abundance

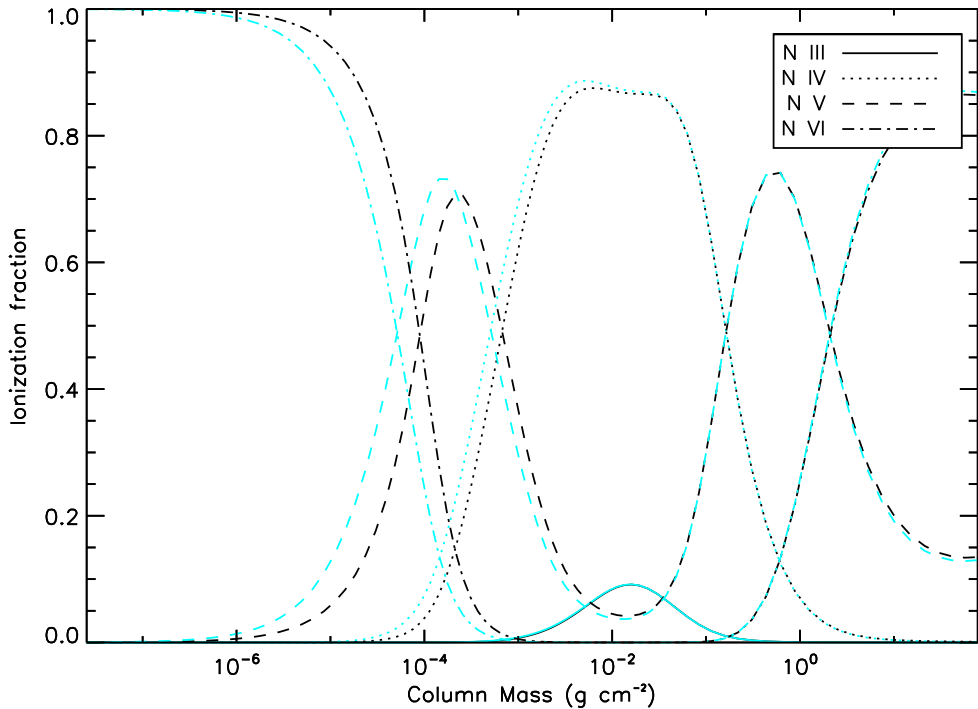


Figure 8. Plot of ionization fraction for N_{IV}–VII for Models 1 (black curve) and 3 (cyan curve). Colour figures are available online.

of $9.88_{-0.21}^{+0.28} \times 10^{-7}$ was measured. For Model 2, we measured the abundance to be $1.22_{-0.04}^{+0.04} \times 10^{-6}$, being a ~ 23 per cent increase from Model 1. For Model 3, only a very small difference was noted. We measured the abundance to be $9.81_{-0.21}^{+0.23} \times 10^{-6}$, which is a <1 per cent decrease. In Model 4, we again see a large increase in the abundance from Model 1, measuring $1.20_{-0.04}^{+0.04} \times 10^{-6}$, which is a ~ 21 per cent increase.

4.2.5 Ionization fraction agreement

In addition to the differences noted above, abundances for different ionization stages of N and O were found to diverge depending upon the PICS or atomic data used. In the case of N, the difference between the N_{IV} and N_V abundances for Model 1 is $0.02_{-0.22}^{+0.22} \times 10^{-7}$, whereas for Models 2, 3, and 4 the differences are $-0.12_{-0.22}^{+0.22} \times 10^{-7}$, $-0.25_{-0.22}^{+0.22} \times 10^{-7}$, and $-0.39_{-0.22}^{+0.22} \times 10^{-7}$, respectively. For O, the difference between the O_{IV} and O_V abundances for Model 1 is $-1.01_{-0.07}^{+0.07} \times 10^{-6}$, whereas for Models 2, 3, and 4 the differences are $-1.11_{-0.07}^{+0.07} \times 10^{-6}$, $-1.25_{-0.08}^{+0.08} \times 10^{-6}$, and $-1.36_{-0.08}^{+0.08} \times 10^{-6}$, respectively. The reason for this can be seen upon inspection of the ionization fractions for N and O. In Figs 8 and 9, we have plotted the ionization fractions for N and O against column mass for Models 1 and 3. In both cases, it can be seen that the Model 3 ionization fractions have been shifted to smaller column masses. In the case of O, this effect is far more pronounced. In addition, it can also be seen that the shift to smaller column masses is larger for N/O_V than it is for N/O_{IV}. Therefore, this explains why the abundance measurements diverge.

Notwithstanding changes to the atomic data and PICS, the overall agreement between abundances measured for different ionization stages of particular species is generally poor. For this work, we adopted $T_{\text{eff}} = 52\,500$ K and $\log g = 7.53$ as measured by Barstow et al. (2003) for G191-B2B for Models 1 to 4. These values were used for consistency with the work described by Preval et al. (2013).

Since then, measurements of T_{eff} and $\log g$ for G191-B2B have been revised upward by Rauch et al. (2013) to 60 000 K and 7.60, respectively. The agreement between abundances measured for different ionization stages is a sensitive function of T_{eff} , atmospheric composition, and to a lesser extent (sans H) $\log g$. Our work was not focused on finding the best combination of T_{eff} , $\log g$, and atmospheric composition, but instead focused on whether a change, if any, occurred to the measured abundances when altering the atomic data and PICS.

4.2.6 Abundance differences

Interestingly, the difference between abundances measured using Models 1 and 4 can be related to the differences between abundances measured using Models 1 and 2, and 1 and 3. For example, the difference between the N_V abundances measured using Models 1 and 2 is $-0.12_{-0.02}^{+0.02} \times 10^{-7}$, whereas for Models 1 and 3, it is $-0.23_{-0.02}^{+0.02} \times 10^{-7}$. If we add these differences from the abundance found in Model 1, we obtain a total of $-0.35_{-0.03}^{+0.03} \times 10^{-7}$. It is for this reason that we include an extra column in Table 7, where the differences between abundances measured using Models 1 and 2, and 1 and 3, are summed together. It can be seen that in all cases, the sum of these is equal to (within the uncertainties) the 1–4 column. This is easily explained in terms of the opacity. Recall that the total opacity in a stellar atmosphere is just a linear sum of each individual contribution. In this case, it is the bound-free (PICS) and the bound-bound (Ku92 or Ku11) that is being added. Model 2 and Model 3 use the Ku11/Hydrogenic PICS and the Ku92/AUTOSTRUCTURE PICS, respectively. Given that Model 1 uses the Ku92/Hydrogenic PICS, subtracting the abundance found in Model 2 from Model 1 shows the effect of including more Ni transitions. Likewise, subtracting the abundance found in Model 3 from Model 1 shows the effect of including more realistic PICS. Therefore, adding these two differences together will give the combination of these two effects. This

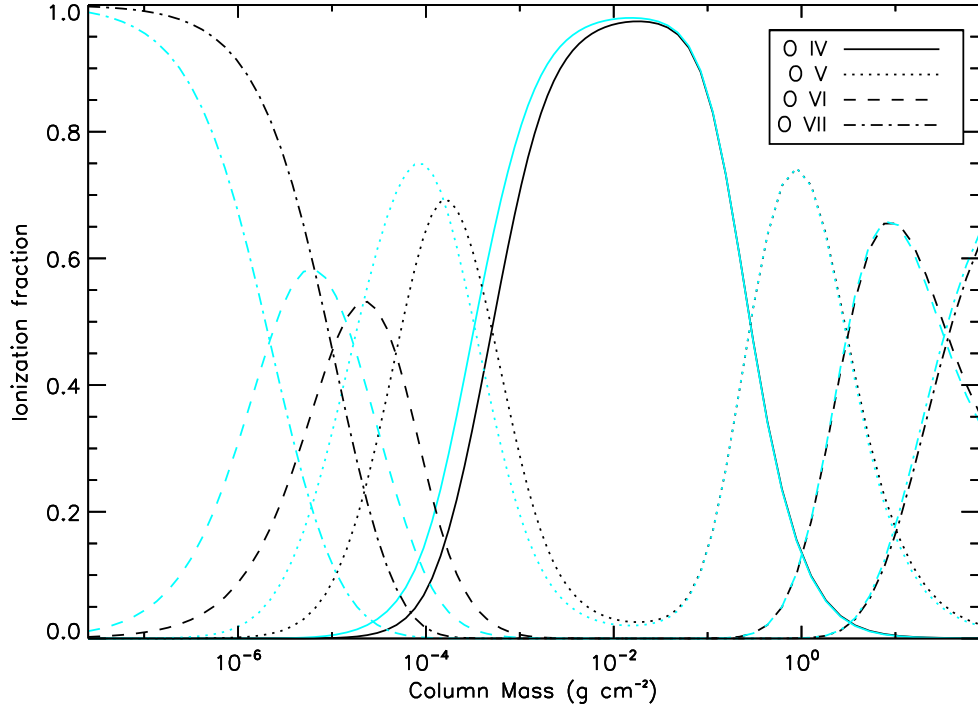


Figure 9. Same as Fig. 8, but for O IV–VII.

explains why statistically significant differences were observed only when using Model 4 for Fe IV–V, in that the effects of both the line list and the PICS combine.

4.3 General discussion

Ideally, any calculation should be as accurate as possible including the most up-to-date data available. However, this also needs to be balanced in terms of time constraints, and the task at hand. We have seen that in the EUV, the choice of using either [Ku92](#) or [Ku11](#) is irrelevant as the change is very small. The shape of the continuum, however, is very sensitive to the PICS used. The downside to using the larger line list from [Ku11](#) increases the calculation time significantly. For example, Model 1 took $\sim 17\,500$ s (292 min) to converge, whereas Model 2 took $\sim 37\,000$ s (617 min). This is because the [Ku11](#) data have more energy levels, and are hence split into a larger number of superlevels than for [Ku92](#) data.

From a wider perspective, the PICS calculated using `AUTOSTRUCTURE` caused the most changes, in that the EUV continuum was severely attenuated, and abundances for N and O were changed. When using the [Ku11](#) line list in model atmospheres, abundances for Ni changed significantly while the continua for various spectral regions were left relatively unchanged. Given that a calculation with [Ku11](#) data takes twice as long to do than with [Ku92](#), an abundance change in only Ni IV–V is relatively little payoff compared to the physics we can learn from changing the PICS. The way forward in improving the quality of future model atmosphere calculations is clear; effort should be focused on improving the PICS data for ions where it exists, as well as filling in gaps where it is required (in this case, for Ni).

This piece of work has been a proof-of-concept endeavour. While we have shown that replacing hydrogenic cross-section data with more realistic calculations has a significant effect on synthesized spectra and measurements, we have only considered direct PI. If a direct PI-only calculation has this large an effect, then it stands to rea-

son that a full calculation including photoexcitation/autoionization resonances will cause a greater effect.

The applications of this work is not limited to WD stars. This data can be used in stellar atmosphere models for objects of any kind, and any temperature range. We chose to demonstrate the effects of our calculations on a hot DA WD star as calculations for these objects are relatively simple. At this temperature regime, we do not need to worry about the effects of 3D modelling, convection etc.

4.4 Future work

As mentioned in our discussion, this work has been a proof-of-concept. The next step is to extend our PICS calculations to include other ions of Ni. Once this is done, we plan to include the omitted resonances to our calculations, and re-examine the effect including this data has on model spectra and measurements.

The present PICS data were calculated using a distorted wave approximation. A potentially more accurate calculation can be achieved using the R-Matrix method as in the OP. Therefore, we aim to do some test calculations to compare Ni PICS using both the R-Matrix or distorted wave approximation.

The EUV spectra of hot metal-polluted WDs has historically been difficult to model (cf. [Lanz et al. 1996](#); [Barstow et al. 1998](#)), the key to which may be the input atomic physics. Therefore, we will also consider the quality of fits to the EUV spectra of several metal-polluted WD stars.

5 CONCLUSION

We have presented our PICS calculations of Ni IV–VI using the distorted wave code `AUTOSTRUCTURE`. We investigated the effect of using two different line lists ([Ku92](#) and [Ku11](#)) and two different sets of PICS (hydrogenic and `AUTOSTRUCTURE`) on synthesized spectra and abundance measurements based on the hot DA WD G191-B2B. This investigation was done by calculating four models (labelled 1, 2, 3,

and 4) with permutations of the Ni line list and PICS used. Model 1 used [Ku92](#) line list/hydrogenic PICS, Model 2 used [Ku11](#) line list/hydrogenic PICS, Model 1 used [Ku92](#) line list/AUTOSTRUCTURE PICS, and Model 4 used [Ku11](#) line list/AUTOSTRUCTURE PICS.

We synthesized model spectra for each of the four models in the EUV, UV, and optical regions. In the EUV, Model 3 showed large attenuation shortward of 180 Å of up to ~ 80 per cent relative to Model 1, whereas Model 2 was relatively unchanged. In the UV, the continuum was unchanged in Models 2 and 3. However, in Model 2, the Ni absorption feature depths changed significant, increasing in depth by up to ~ 10 per cent. Absorption features in Model 3 were relatively unchanged, with depth changes of ~ 3 per cent across the spectrum. In the optical, changes in flux were so small (<0.1 per cent) across models that these are unlikely to be observed, nor would it be possible to differentiate between them. Model 4 was not plotted in the EUV, UV, or optical as the resultant spectrum was just a combination of the effects observed in Models 2 and 3.

We measured metal abundances for G191-B2B using all four models. This was to see if there were any differences in the metal abundances measured when changing the PICS or atomic data included in the model calculation. Statistically significant (consistent with non-zero difference compared to Model 1) abundance changes were observed in N v over all models, and O IV–v when using Models 3 and 4. This suggests that the N abundances are sensitive to both the line list and PICS used, while the O abundances were only sensitive to the PICS. The Fe IV–v abundances only changed by a statistically significant amount for Model 4, implying a combination of the line list and cross-section caused the change. The Ni IV–v abundances changed by a statistically significant amount for Models 2 and 4, implying the line list caused the difference. Interestingly, for each metal abundance, the difference between measurements made using Models 1 and 4 could be found by summing the differences between measurements made using Models 1 and 2, and Models 1 and 3. This is in keeping with the assumption that predicted radiation for small variations of the opacity sources scales roughly linearly with the opacity.

In addition, we found the abundances of N/O IV and v diverged depending on the PICS used. A comparison of the ionization fractions calculated using Models 1 and 3 showed that the charge states for Model 3 formed higher in the atmosphere than the charge states for Model 1. Furthermore, N/O v experiences a larger change with respect to depth formation than N/O IV, explaining the divergence of the abundance measurements.

Our work has demonstrated that, even with a limited calculation, the Ni PICS have made a significant difference to the synthetic spectra, and by extension what is measured from observational data.

Comparatively, an extended line list such as [Ku11](#) offers little benefit given the extended computational time required to converge a model atmosphere, and the small pay off (changed Ni abundance). It is our opinion that future atomic data calculations for stellar atmosphere models should not necessarily focus on how big the line list is, but the quality of the PICS.

ACKNOWLEDGEMENTS

We gratefully acknowledge the time and effort expended by Robert Kurucz in assisting with this project. We also thank Simon Jeffrey and Nigel Bannister for helpful discussions. SPP and MAB acknowledge the support of an STFC student grant.

REFERENCES

Anderson L. S., 1989, *ApJ*, 339, 558
 Arnaud K. A., 1996, in Jacoby G. H., Barnes J., eds, *ASP Conf. Ser. Vol. 101, Astronomical Data Analysis Software and Systems V*. Astron. Soc. Pac., San Francisco, p. 17
 Badnell N. R., 1986, *J. Phys. B*, 19, 3827
 Badnell N. R., 1997, *J. Phys. B*, 30, 1
 Badnell N. R., 2011, *Comput. Phys. Commun.*, 182, 1528
 Barstow M. A., Hubeny I., Holberg J. B., 1998, *MNRAS*, 299, 520
 Barstow M. A., Good S. A., Holberg J. B., Hubeny I., Bannister N. P., Bruhweiler F. C., Burleigh M. R., Napiwotzki R., 2003, *MNRAS*, 341, 870
 Chayer P., Fontaine G., Wesemael F., 1995, *ApJS*, 99, 189
 Cowan R. D., 1981, *Los Alamos Series in Basic and Applied Sciences*. Univ. California Press, Berkeley
 Eissner W., Nussbaumer H., 1969, *J. Phys. B*, 2, 1028
 Holberg J. B., Hubeny I., Barstow M. A., Lanz T., Sion E. M., Tweedy R. W., 1994, *ApJ*, 425, L105
 Hubeny I., 1988, *Comput. Phys. Commun.*, 52, 103
 Hubeny I., Lanz T., 1995, *ApJ*, 439, 875
 Hubeny I., Lanz T., 2011, *Astrophysics Source Code Library*, record ascl:1109.022
 Kurucz R. L., 1992, *Rev. Mex. Astron. Astrofis.*, 23, 45 ([Ku92](#))
 Kurucz R. L., 2011, *Can. J. Phys.*, 89, 417 ([Ku11](#))
 Lanz T., Barstow M. A., Hubeny I., Holberg J. B., 1996, *ApJ*, 473, 1089
 Preval S. P., Barstow M. A., Holberg J. B., Dickinson N. J., 2013, *MNRAS*, 436, 659
 Rauch T., Werner K., Bohlin R., Kruk J. W., 2013, *A&A*, 560
 Seaton M. J., Badnell N. R., 2004, *MNRAS*, 354, 457
 Vennes S., Lanz T., 2001, *ApJ*, 553, 399
 Werner K., Dreizler S., 1994, *A&A*, 286, L31

This paper has been typeset from a $\text{\TeX}/\text{\LaTeX}$ file prepared by the author.